

An Iterative Least-Squares Method for the Hyperbolic Monge-Ampère Equation with Transport Boundary Condition

M.W.M.C. Bertens^{1,*}, M.J.H. Anthonissen¹,
J.H.M. ten Thije Boonkkamp¹, and W.L. IJzerman^{1,2}

¹*CASA, Department of Mathematics and Computer Science, Eindhoven University of Technology, PO Box 513, 5600 MB Eindhoven, The Netherlands*

²*Signify Research, High Tech Campus 7, 5656 AE Eindhoven, The Netherlands*

*Corresponding author: m.w.m.c.bertens@tue.nl

Keywords— Hyperbolic Monge-Ampère equation, Transport boundary condition, Iterative least-squares method

Abstract

A least-squares method for solving the hyperbolic Monge-Ampère equation with transport boundary condition is introduced. The method relies on an iterative procedure for the gradient of the solution, the so-called mapping. By formulating error functionals for the interior domain, the boundary, both separately and as linear combination, three minimization problems are solved iteratively to compute the mapping. After convergence, a fourth minimization problem, to compute the solution of the Monge-Ampère equation, is solved. The approach is based on a least-squares method for the elliptic Monge-Ampère equation [1], and is improved upon by the addition of analytical solutions for the minimization on the interior domain and by the introduction of two new boundary methods. Lastly, the iterative method is tested on a variety of examples. It is shown that, when the iterative method converges, second-order global convergence as function of the spatial discretization is obtained.

1 Introduction

In this paper we introduce a least-squares method for the hyperbolic Monge-Ampère equation with transport boundary condition. We are motivated by appli-

cations to optical design. In [2] it was found that designing lenses and reflectors for some single-optical-surface systems is equivalent to solving the Monge-Ampère (MA) equation with transport boundary condition. The optical surface satisfies either the elliptic (+) or hyperbolic (-) MA equation, i.e.,

$$\det(\mathbf{D}^2u(\mathbf{x})) = \pm \frac{E(\mathbf{x})}{I(\nabla u(\mathbf{x}))}, \quad \mathbf{x} \in \mathcal{X}, \quad (1a)$$

where \mathbf{D}^2u is the Hessian matrix of the optical surface $z = u(\mathbf{x})$, $E \geq 0$ the emittance of the source with domain $\mathcal{X} \subset \mathbb{R}^2$ and $I > 0$ the illuminance on the target with domain $\mathcal{Y} = \nabla u(\mathcal{X}) \subset \mathbb{R}^2$. The accompanying transport boundary condition is given by

$$\nabla u(\partial\mathcal{X}) = \partial\mathcal{Y}. \quad (1b)$$

In the elliptic case this boundary condition follows from convexity or concavity arguments of the optical surface [2]. For the hyperbolic MA equation, the transport boundary condition cannot be derived in the same manner as $z = u(\mathbf{x})$ is a saddle surface, and one instead relies on optical arguments, e.g., the edge-ray principle [3]. Further disparities between the elliptic and hyperbolic variant are common. This for one is due to the connection of the elliptic variant to the rich field of optimal transport (OT) [4, p. 282], which is absent for the hyperbolic MA equation. OT was originally established by Monge, who was concerned with rearranging mass from one distribution to another [5, p. xiv]. Brenier proved that, assuming regularity conditions [6], the corresponding optimal (point-wise) transport map $\mathbf{m} = \nabla u$ satisfies the elliptic Monge-Ampère equation (1a), where the plus sign is assumed and E and I should be interpreted as densities. See [4, p. 323-332], for example, for regularity, uniqueness and existence of solutions to the elliptic MA equation. Assumptions on energy conservation allow design of optical systems to be cast in the framework of OT, but only for the elliptic variant and not for the hyperbolic MA equation. As a consequence, results regarding regularity, uniqueness and existence for the hyperbolic MA equation are scarce. The most relevant results for the hyperbolic MA equation

$$\det(\mathbf{D}^2u(\mathbf{x})) = -f^2(\mathbf{x}), \quad \mathbf{x} \in \mathcal{X} \subset \mathbb{R}^2, \quad (2)$$

with $f : \mathbb{R}^2 \mapsto (0, \infty)$, follow from the method of characteristics [7, 8] and only hold for Cauchy boundary conditions. Equation (2) has received little interest in numerical and computational journals. To the best of our knowledge, the equation has been solved twice, once on a triangular computational domain [9, p. 614] and secondly on a rectangular computational domain by Bertens et al. [10]. The former method, based on a finite difference scheme, assumes Cauchy boundary conditions on an initial curve, and does not treat boundary conditions on the rest of the domain. The latter method, derived using the method of characteristics, shows that the requirements on the boundary conditions are strenuous. The method of

characteristics shows, by parametrizing the characteristics with the x -coordinate and assuming Cauchy boundary conditions on an initial curve $x = \text{const}$, that the remaining boundary conditions depend on the location of the characteristics. Consequently, the required boundary conditions are fundamentally different from the transport boundary condition.

In this work, we therefore do not consider the method of characteristics, but instead resort to a least-squares method which has been proven to work for various elliptic problems, among which the Monge-Ampère equation [1], the generalized Monge-Ampère equation and the generated Jacobian equation [11]. The least-squares algorithm is an iterative method which does not directly solve for the unknown u , but instead first constructs the mapping $\mathbf{m} = \nabla u$ and afterwards approximates u . The general outline of the least-squares method is as follows: first, we approximate the Jacobi matrix of \mathbf{m} in the interior of the domain by minimizing an error functional. Secondly, \mathbf{m} restricted to the boundary of the domain is approximated. By minimizing another error functional involving the newly found Jacobi matrix and the boundary approximation, we obtain a new approximation for the mapping. We proceed by repeating these three steps iteratively until \mathbf{m} no longer changes and subsequently calculate u by minimizing a fourth functional. One of the benefits of this method is that each of the three stages can be adapted for the problem at hand. For example, the minimization for \mathbf{m} in [1] relies on a finite difference scheme while in [12] it uses a finite volume scheme. This three-stage approach allows us to introduce two new boundary methods, viz. a *segmented projection method* and a *segmented arc length method*, which both lead to better results and higher computational efficiency than the original *projection method* [1]. Even more importantly, the iterative method using the *segmented projection method* converges in some cases when the original *projection method* does not. And, as we will show, the *segmented arc length method* converges for all examples. Furthermore, we improve upon the first minimization procedures, viz. the procedure for approximating the Jacobi matrix in the interior of the domain. Numerical experiments have shown that grid lines in target space can intersect, preventing proper numerical convergence of our algorithm. Therefore, we introduce a method to prevent these so-called grid shocks.

The content of this paper is as follows. We discuss the theory of the least-squares method for the Monge-Ampère equation in Section 2. In Section 2.1 the least-squares method is introduced. Afterwards, we adapt part of the method, viz. the optimization in the interior domain, in Section 2.2. Next, in Section 2.3, we introduce various boundary methods to replace the existing projection method and in Section 2.4 we introduce a grid shock correction method. In Section 3 we compare the boundary methods, show their weaknesses and strengths and elaborate on the convergence of the algorithm for various test cases. Lastly, we end with a discussion of the results followed by conclusions in Section 4.

2 The least-squares formulation

We are interested in the two-dimensional hyperbolic Monge-Ampère equation with transport boundary condition, given by

$$\det(\mathbf{D}^2u(\mathbf{x})) + f^2(\mathbf{x}, \nabla u(\mathbf{x})) = 0, \quad \mathbf{x} \in \mathcal{X}, \quad (3a)$$

$$\nabla u(\partial\mathcal{X}) = \partial\mathcal{Y}, \quad (3b)$$

where $u = u(\mathbf{x})$ is the unknown, \mathbf{D}^2u the Hessian matrix of u , $f^2 > 0$ and $\mathcal{X}, \mathcal{Y} \subset \mathbb{R}^2$ connected domains. We require the boundaries $\partial\mathcal{X}$ and $\partial\mathcal{Y}$ to be orientable. The transport boundary condition (3b) can be interpreted as

$$\begin{cases} \forall \mathbf{x} \in \partial\mathcal{X} : \nabla u(\mathbf{x}) \in \partial\mathcal{Y}, \\ \forall \mathbf{y} \in \partial\mathcal{Y} \exists \mathbf{x} \in \partial\mathcal{X} : \nabla u(\mathbf{x}) = \mathbf{y}, \end{cases} \quad (4a)$$

where the latter condition is recognized as surjectivity of ∇u . Bijectivity is generally not implied, not even when restricted to the boundary, as will become apparent by the example discussed in Section 3.4. Hyperbolicity of (3a) follows from the discriminant of the characteristic condition, which can be obtained by rewriting (3a) as

$$F(\mathbf{x}, u, p, q, r, s, t) = rt - s^2 + f^2 = 0, \quad (5)$$

where $p = u_{x_1}$, $q = u_{x_2}$, $r = u_{x_1x_1}$, $s = u_{x_1x_2}$ and $t = u_{x_2x_2}$. The characteristic condition is given by [10, p. 10]

$$F_r\mu^2 - F_s\mu + F_t = 0, \quad (6)$$

for the unknown function μ , representing the slope of the characteristics. For the MA equation to be hyperbolic, two real characteristics need to exist for every point in the domain, hence the slopes of the two characteristics, and thus the roots of (6), need to be real and distinct. Henceforth, the discriminant of (6) should be strictly positive. It follows that the discriminant Δ of (6) is given by

$$\Delta = F_s^2 - 4F_rF_t = 4s^2 - 4tr = 4f^2, \quad (7)$$

which is, by assumption, strictly positive. Hence, equation (3a) is hyperbolic.

2.1 Least-squares approach

In [1] a least-squares method was introduced to solve the elliptic Monge-Ampère equation given by $\det(\mathbf{D}\mathbf{m}) = f^2(\mathbf{x}, \nabla u(\mathbf{x}))$ for $\mathbf{x} \in \mathcal{X}$ and $\mathbf{D}\mathbf{m}$ the Jacobi matrix of \mathbf{m} . The main idea of the least-squares method is to reformulate the Monge-Ampère equation in terms of the mapping $\mathbf{m} : \mathcal{X} \rightarrow \mathcal{Y}$, representing ∇u , and solve for \mathbf{m} . Subsequently, u is reconstructed from \mathbf{m} in a least-squares sense. To

solve the hyperbolic problem we replace the right-hand side of the elliptic Monge-Ampère equation by $-f^2(\mathbf{x}, \nabla u(\mathbf{x}))$ and substitute $\mathbf{D}\mathbf{m} = \mathbf{D}^2u$, thus obtaining

$$\det(\mathbf{D}\mathbf{m}(\mathbf{x})) + f^2(\mathbf{x}, \mathbf{m}(\mathbf{x})) = 0, \quad \mathbf{x} \in \mathcal{X}, \quad (8a)$$

$$\mathbf{m}(\partial\mathcal{X}) = \partial\mathcal{Y}. \quad (8b)$$

We formulate a minimization problem for \mathbf{m} which we solve numerically. For this, we introduce the auxiliary functions $\mathbf{P} : \mathcal{X} \rightarrow \mathbb{R}^{2 \times 2}$ and $\mathbf{b} : \partial\mathcal{X} \rightarrow \partial\mathcal{Y}$ which are used to approximate $\mathbf{D}\mathbf{m}$ on the whole domain and \mathbf{m} on the boundary, respectively. This is achieved by the least-squares method, i.e., subsequently minimizing three separate functionals given by

$$J_I(\mathbf{m}, \mathbf{P}) = \frac{1}{2} \iint_{\mathcal{X}} \|\mathbf{D}\mathbf{m} - \mathbf{P}\|^2 \, d\mathbf{x}, \quad (9a)$$

$$J_B(\mathbf{m}, \mathbf{b}) = \frac{1}{2} \oint_{\partial\mathcal{X}} |\mathbf{m} - \mathbf{b}|^2 \, ds, \quad (9b)$$

$$J(\mathbf{m}, \mathbf{P}, \mathbf{b}) = \alpha J_I(\mathbf{m}, \mathbf{P}) + (1 - \alpha) J_B(\mathbf{m}, \mathbf{b}), \quad (9c)$$

where $|\cdot|$ is the standard 2-norm, $\|\cdot\|$ is the Frobenius norm defined by $\|\mathbf{A}\|^2 = \text{Tr}(\mathbf{A}\mathbf{A}^T)$ for a matrix \mathbf{A} and $0 < \alpha < 1$ is a control parameter to either place weights on the boundary and the interior. Starting with an initial guess \mathbf{m}^0 , the iterative optimization procedure for $n = 0, 1, 2, \dots$ reads

$$\mathbf{P}^{n+1} = \underset{\mathbf{P} \in \mathcal{P}(\mathbf{m}^n)}{\text{argmin}} J_I(\mathbf{m}^n, \mathbf{P}), \quad (10a)$$

$$\mathbf{b}^{n+1} = \underset{\mathbf{b} \in \mathcal{B}}{\text{argmin}} J_B(\mathbf{m}^n, \mathbf{b}), \quad (10b)$$

$$\mathbf{m}^{n+1} = \underset{\mathbf{m} \in \mathcal{V}}{\text{argmin}} J(\mathbf{m}, \mathbf{P}^{n+1}, \mathbf{b}^{n+1}). \quad (10c)$$

The spaces $\mathcal{P}(\mathbf{m}^n)$, \mathcal{B} and \mathcal{V} follow from three key observations. First, because $\mathbf{m} = \nabla u$, the Jacobi matrix $\mathbf{D}\mathbf{m} = \mathbf{D}^2u$ is symmetric and $\det(\mathbf{D}\mathbf{m}) = -f^2(\mathbf{x}, \mathbf{m}(\mathbf{x}))$. Secondly, by the transport boundary condition, for all $\mathbf{x} \in \partial\mathcal{X} : \mathbf{m}(\mathbf{x}) \in \partial\mathcal{Y}$. As we require \mathbf{m} to be twice continuously differentiable later on, we impose this requirement. The three sets are then given by

$$\mathcal{P}(\mathbf{m}) = \{\mathbf{P} \in [C^1(\mathcal{X})]^{2 \times 2} \mid \det(\mathbf{P}(\mathbf{x})) = -f^2(\mathbf{x}, \mathbf{m}(\mathbf{x})), \mathbf{P} = \mathbf{P}^T\}, \quad (11a)$$

$$\mathcal{B} = \{\mathbf{b} \in [C(\partial\mathcal{X})]^2 \mid \mathbf{b}(\mathbf{x}) \in \partial\mathcal{Y}\}, \quad (11b)$$

$$\mathcal{V} = [C^2(\mathcal{X})]^2. \quad (11c)$$

We first outline the minimization of J , as it remains unchanged w.r.t. [1], and in the next sections we elaborate on the minimization of J_I and J_B . Taking the variational derivative of (9c) and applying the fundamental lemma of calculus of

variations [13, p. 185] yields that for the optimal \mathbf{m} , each of its components should satisfy a Poisson equation with Robin boundary condition given by

$$\Delta m_1 = \nabla \cdot \mathbf{p}_1, \quad \mathbf{x} \in \mathcal{X}, \quad (12a)$$

$$(1 - \alpha)m_1 + \alpha \nabla m_1 \cdot \hat{\mathbf{n}} = (1 - \alpha)b_1 + \alpha \mathbf{p}_1 \cdot \hat{\mathbf{n}}, \quad \mathbf{x} \in \partial\mathcal{X}, \quad (12b)$$

for the first component m_1 and

$$\Delta m_2 = \nabla \cdot \mathbf{p}_2, \quad \mathbf{x} \in \mathcal{X}, \quad (13a)$$

$$(1 - \alpha)m_2 + \alpha \nabla m_2 \cdot \hat{\mathbf{n}} = (1 - \alpha)b_2 + \alpha \mathbf{p}_2 \cdot \hat{\mathbf{n}}, \quad \mathbf{x} \in \partial\mathcal{X}, \quad (13b)$$

for the second component m_2 . The functions \mathbf{p}_i ($i = 1, 2$) denote the i^{th} column of the matrix \mathbf{P} and $\hat{\mathbf{n}}$ is the unit outward normal vector to $\partial\mathcal{X}$.

Upon convergence of (10) we reconstruct u from \mathbf{m} by minimizing another least-squares functional, viz.

$$u = \operatorname{argmin}_{\psi \in C^2(\mathcal{X})} \frac{1}{2} \iint_{\mathcal{X}} |\nabla \psi - \mathbf{m}|^2 \, d\mathbf{x}. \quad (14)$$

Using calculus of variations once more, we obtain the Poisson equation with Neumann boundary conditions for u , which reads

$$\Delta u = \nabla \cdot \mathbf{m}, \quad \mathbf{x} \in \mathcal{X}, \quad (15a)$$

$$\nabla u \cdot \hat{\mathbf{n}} = \mathbf{m} \cdot \hat{\mathbf{n}}, \quad \mathbf{x} \in \partial\mathcal{X}. \quad (15b)$$

For (15) to admit a solution, the compatibility condition [14, p. 184]

$$\iint_{\mathcal{X}} \nabla \cdot \mathbf{m} \, d\mathbf{x} - \oint_{\partial\mathcal{X}} \mathbf{m} \cdot \hat{\mathbf{n}} \, ds = 0, \quad (16)$$

is automatically satisfied due to the divergence theorem.

We solve the three Poisson equations using finite differences (FD), more specifically, standard second-order central differences for both the first and second order derivatives. For grid points on the boundary we introduce ghost points, which we eliminate using the normal derivatives in the Robin boundary condition. The system we obtain from discretizing (12) and (13) needs to be solved in each iteration. In order to increase computational efficiency, we compute the LU-decomposition in the initialization of the algorithm. Note that the solution for u is not unique due to the (transport) boundary condition [15, p. A1438], which is also reflected by (15b), so we enforce uniqueness by fixing one function value of u , i.e., let $\mathbf{x} \in \mathcal{X}$ be arbitrary, we then impose the condition $u(\mathbf{x}) = 0$. In practice we assume $\mathcal{X} = [x_m, x_M] \times [y_m, y_M]$ and we impose $u(x_m, y_m) = 0$. Alternatively, one could prescribe the average value of u on the domain [16, p. 177].

2.2 P-optimization

The matrix \mathbf{Dm} cannot be determined exactly during the iterative process. Because the integrand of J_1 , i.e., $\|\mathbf{Dm} - \mathbf{P}\|^2$, does not depend on derivatives of \mathbf{P} we employ a piece-wise minimization. To this end we approximate \mathbf{Dm} using standard finite difference. Let $\mathbf{x}_{ij} = ((x_1)_i, (x_2)_j) \in \mathcal{X}$ be the grid points of a Cartesian grid with $i = 1, \dots, N_{x_1}$ and $j = 1, \dots, N_{x_2}$ denoting the first and second coordinate, respectively. We write $\mathbf{m}_{ij} \approx \mathbf{m}(\mathbf{x}_{ij})$ and similar for the other variables. We approximate $(\mathbf{Dm})_{ij}$ by \mathbf{D}_{ij} using central and one-sided second-order finite differences in the interior and at the boundary, respectively. This implies that \mathbf{D} is in general not symmetric, while \mathbf{Dm} and \mathbf{P} are. By virtue of the point-wise minimization we proceed to drop the subscripts, e.g., we write \mathbf{m} instead of \mathbf{m}_{ij} , for brevity.

Let $F(p_{11}, p_{22}, p_{12}) = \|\mathbf{D} - \mathbf{P}\|^2$; expanding it yields

$$F(p_{11}, p_{22}, p_{12}) = \frac{1}{2} \left((p_{11} - d_{11})^2 + (p_{12} - d_{12})^2 + (p_{12} - d_{21})^2 + (p_{22} - d_{22})^2 \right). \quad (17)$$

We replace \mathbf{D} by its symmetric part $\mathbf{D}_s = \frac{1}{2}(\mathbf{D} + \mathbf{D}^T)$, or written in its components, we introduce $d_s = \frac{1}{2}(d_{12} + d_{21})$ and

$$\mathbf{D}_s = \begin{pmatrix} d_{11} & d_s \\ d_s & d_{22} \end{pmatrix}. \quad (18)$$

Furthermore, we replace F by $F_s = \frac{1}{2}\|\mathbf{P} - \mathbf{D}_s\|^2$, i.e.,

$$F_s(p_{11}, p_{22}, p_{12}) = \frac{1}{2} \left((p_{11} - d_{11})^2 + 2(p_{12} - d_s)^2 + (p_{22} - d_{22})^2 \right). \quad (19)$$

To justify the replacement, note that

$$F(p_{11}, p_{22}, p_{12}) = F_s(p_{11}, p_{22}, p_{12}) + \frac{1}{4}(d_{12} - d_{21})^2, \quad (20)$$

hence, (p_{11}, p_{22}, p_{12}) minimizes F if and only if it minimizes F_s . To obtain the minimizers, we minimize F_s under the condition $\mathbf{P} \in \mathcal{P}(\mathbf{m})$ using Lagrange multipliers. The Lagrangian is thus given by

$$\Lambda(p_{11}, p_{22}, p_{12}, \lambda) = F_s(p_{11}, p_{22}, p_{12}) + \lambda (p_{11}p_{22} - p_{12}^2 + f^2). \quad (21)$$

By setting the partial derivatives of Λ with respect to p_{11} , p_{22} , p_{12} and λ to zero, we find that the critical points of Λ have to satisfy

$$p_{11} + \lambda p_{22} = d_{11}, \quad (22a)$$

$$\lambda p_{11} + p_{22} = d_{22}, \quad (22b)$$

$$(1 - \lambda)p_{12} = d_s, \quad (22c)$$

$$p_{11}p_{22} - p_{12}^2 = -f^2. \quad (22d)$$

This system can be solved analytically and the results are given by Prins et al. [1, p. B942-B947] for the elliptic Monge-Ampère equation, with $-f^2$ replaced by f^2 in (22d). Unfortunately, the list of solutions is not complete as for the case $d_{11} = -d_{22}$, two roots of (22) are missing. We propose a different solution strategy here. First, two remarks are in place. While minimizing F_s , the matrix \mathbf{D}_s and the function value of f are given and both \mathbf{P} and λ have to be computed. Hence, we provide a classification in terms of \mathbf{D}_s and the corresponding solutions of (22). Furthermore, because the matrix \mathbf{D}_s is an approximation, $\det(\mathbf{D}_s) \neq -f^2$ and in general $\det(\mathbf{D}_s) \geq 0$ could possibly occur. We first write the linear equations of (22) as

$$\mathbf{A}\mathbf{p} = \mathbf{d}, \quad \mathbf{A} = \begin{pmatrix} 1 & \lambda & 0 \\ \lambda & 1 & 0 \\ 0 & 0 & 1 - \lambda \end{pmatrix}, \quad \mathbf{p} = \begin{pmatrix} p_{11} \\ p_{22} \\ p_{12} \end{pmatrix}, \quad \mathbf{d} = \begin{pmatrix} d_{11} \\ d_{22} \\ d_{12} \end{pmatrix}. \quad (23)$$

The vector \mathbf{p} is uniquely determined when \mathbf{A} is regular, i.e., when $0 \neq \det(\mathbf{A}) = (1 - \lambda)^2(1 + \lambda)$. We should therefore distinguish between the cases $\lambda = 1$, $\lambda = -1$ and $\lambda \neq \pm 1$.

Although we should consider the cases $\lambda = 1$, $\lambda = -1$ and $\lambda \neq \pm 1$ separately, \mathbf{d} and f are given and λ and \mathbf{p} are to be calculated. Therefore we consider three cases based on \mathbf{D}_s , viz., **Case 1:** $d_{11} = d_{22}$ and $d_s = 0$, **Case 2:** $d_{11} = -d_{22}$ and **Case 3:** all other \mathbf{D}_s . We consider $\mathbf{D}_s = \mathbf{0}$ as a special case of $d_{11} = d_{22}$ and $d_s = 0$.

We start with some general results, to be used in the subsequent derivations. First, let $\text{Tr}(\mathbf{A})$ denote the trace of a matrix \mathbf{A} . Using (22) we find

$$\delta_s := \det(\mathbf{D}_s) = \lambda \text{Tr}(\mathbf{P})^2 - (\lambda - 1)^2 f^2, \quad (24a)$$

$$\text{Tr}(\mathbf{D}_s) = (\lambda + 1) \text{Tr}(\mathbf{P}). \quad (24b)$$

Solving the second equation for $\text{Tr}(\mathbf{P})$ and subsequently substituting it in the first equation yields

$$f^2(\lambda^2 - 1)^2 + \delta_s(\lambda + 1)^2 - \text{Tr}(\mathbf{D}_s)^2 \lambda = 0. \quad (25)$$

Next, we consider the roots of (25) and the corresponding solutions \mathbf{P} .

Case 1: $d_{11} = d_{22}$ and $d_s = 0$, which we write as $\mathbf{D}_s = d\mathbf{I}$ with $d \in \mathbb{R}$. We will show that this condition is equivalent with $\lambda = 1$. So, let $\mathbf{D}_s = d\mathbf{I}$. We show that $\lambda = 1$ by forcing a contradiction, so, assume $\lambda \neq 1$. Then subtracting (22a) from (22b) gives $p_{11} = p_{22}$ and by (22c) we have $p_{12} = 0$. Substitution of $p_{11} = p_{22}$ and $p_{12} = 0$ in (22d) yields $p_{11}^2 = -f^2 < 0$, being a contradiction. Therefore $\lambda = 1$. Conversely, substitution of $\lambda = 1$ in \mathbf{A} gives

$$\mathbf{A} = \begin{pmatrix} 1 & 1 & 0 \\ 1 & 1 & 0 \\ 0 & 0 & 0 \end{pmatrix}. \quad (26)$$

In this case the null space of $\mathbf{\Lambda}$ is given by $\mathcal{N}(\mathbf{\Lambda}) = \langle \mathbf{v}_1, \mathbf{v}_2 \rangle$ with $\mathbf{v}_1 = (1, -1, 0)^\top$ and $\mathbf{v}_2 = (0, 0, 1)^\top$. So $\mathbf{\Lambda}\mathbf{p} = \mathbf{d}$ only has a solution if \mathbf{d} lies in the column space of $\mathbf{\Lambda}$, i.e., if $d_{11} = d_{22}$ and $d_s = 0$ or $\mathbf{D}_s = d\mathbf{I}$ with $d \in \mathbb{R}$. Henceforth we have that $\lambda = 1$ is equivalent with $\mathbf{D}_s = d\mathbf{I}$ and thus $\lambda = 1$ only occurs in **Case 1**. The general solution to $\mathbf{\Lambda}\mathbf{p} = \mathbf{d}$ is now given by

$$\mathbf{p} = (p, d - p, 0)^\top + \mu_1 \mathbf{v}_1 + \mu_2 \mathbf{v}_2, \quad p, \mu_1, \mu_2 \in \mathbb{R}. \quad (27)$$

We aim to minimize F_s . Substitution of (27) in F_s gives

$$F_s(p_{11}, p_{22}, p_{12}) = \frac{1}{2} \left((p + \mu_1 - d)^2 + 2\mu_2^2 + (p + \mu_1)^2 \right), \quad (28)$$

thus showing $\mu_2 = 0$. Furthermore, the minimum is independent of the choice for μ_1 as can be seen by writing $\mathbf{p} = (\tilde{p}, d - \tilde{p}, 0)^\top$ with $\tilde{p} = p + \mu_1$. For simplicity we choose $\mu_1 = 0$. Subsequent substitution of \mathbf{p} into (22d) gives $p(d - p) = -f^2$. This second order polynomial in p has two real roots, viz.

$$p = \frac{1}{2} \left(d \pm \sqrt{d^2 + 4f^2} \right). \quad (29)$$

So in total we find the two solutions

$$p_{11} = \frac{1}{2} \left(d \pm \sqrt{d^2 + 4f^2} \right), \quad p_{22} = d - p_{11}, \quad p_{12} = 0. \quad (30)$$

In case $d = 0$, i.e., in case $\mathbf{D}_s = \mathbf{0}$, the above derivation still holds so we consider $\mathbf{D}_s = \mathbf{0}$ an instance of **Case 1**.

Case 2: $d_{11} = -d_{22}$, which we write as $\mathbf{d} = (d, -d, d_s)^\top$ with $d, d_s \in \mathbb{R}$. We have that $\text{Tr}(\mathbf{D}_s) = 0$ and $\delta_s = -(d^2 + d_s^2)$. For this case the fourth order polynomial (25) can be written as

$$(\lambda + 1)^2 \left((\lambda - 1)^2 + \frac{\delta_s}{f^2} \right) = 0. \quad (31)$$

It follows that we have the three unique roots, $\lambda = -1$ (with multiplicity 2) and $\lambda = 1 \pm \sqrt{|\delta_s|}/f$.

- In case $\lambda = -1$ we have

$$\mathbf{\Lambda} = \begin{pmatrix} 1 & -1 & 0 \\ -1 & 1 & 0 \\ 0 & 0 & 2 \end{pmatrix}, \quad (32)$$

and the corresponding null space $\mathcal{N}(\mathbf{\Lambda}) = \langle \mathbf{v}_3 \rangle$ with $\mathbf{v}_3 = (1, 1, 0)^\top$. For \mathbf{p} to be a solution to $\mathbf{\Lambda}\mathbf{p} = \mathbf{d}$ we require \mathbf{d} to be in the column space of $\mathbf{\Lambda}$. It follows that $\mathbf{d} = (d, -d, d_s)^\top$, $d, d_s \in \mathbb{R}$. Henceforth $\lambda = -1$ only occurs for **Case 2**.

The general solution to $\mathbf{\Lambda}\mathbf{p} = \mathbf{d}$ is therefore given by

$$\mathbf{p} = (p, p - d, \frac{1}{2}d_s)^T + \mu_3\mathbf{v}_3, \quad p, \mu_3 \in \mathbb{R}. \quad (33)$$

Writing $\mathbf{p} = (\tilde{p}, \tilde{p} - d, \frac{1}{2}d_s)^T$ with $\tilde{p} = p + \mu_3$ shows that the actual solution \mathbf{p} does not change by choosing μ_3 , so we simply choose $\mu_3 = 0$. By (22d) it follows that

$$p(p - d) - \frac{1}{4}d_s^2 + f^2 = 0. \quad (34)$$

Consequently, solving for p we find that for $|\delta_s| - 4f^2 \geq 0$ we have

$$p_{11} = \frac{1}{2} \left(d \pm \sqrt{|\delta_s| - 4f^2} \right), \quad p_{22} = p_{11} - d, \quad p_{12} = \frac{1}{2}d_s. \quad (35)$$

When $|\delta_s| - 4f^2 < 0$ the solution \mathbf{p} is complex. Because we are only interested in real-valued solutions, we do not consider $\lambda = -1$ when $|\delta_s| - 4f^2 < 0$.

- In the case $\lambda = 1 \pm \sqrt{|\delta_s|}/f$, the matrix $\mathbf{\Lambda}^{-1}$ is uniquely defined (see (37) for an explicit expression) and by $\mathbf{p} = \mathbf{\Lambda}^{-1}\mathbf{d}$ we obtain

$$p_{11} = \mp \frac{df}{\sqrt{|\delta_s|}}, \quad p_{22} = -p_{11}, \quad p_{12} = \mp \frac{d_s f}{\sqrt{|\delta_s|}}. \quad (36)$$

The solutions (36) are new with respect to those found by Prins et al. [1] and are not specific to the hyperbolic Monge-Ampère equation.

Case 3: All other \mathbf{D}_s , i.e., both $\mathbf{D}_s \neq d\mathbf{I}$ and $\mathbf{d}_s \neq (d, -d, d_s)^T$ for all $d, d_s \in \mathbb{R}$. By **Case 1** we have $\lambda \neq 1$ and by **Case 2** we have $\lambda \neq -1$. Therefore $\det \mathbf{\Lambda} = (1 - \lambda)^2(1 + \lambda) \neq 0$. Consequently $\mathbf{\Lambda}$ is invertible and its inverse is given by

$$\mathbf{\Lambda}^{-1} = \frac{1}{1 - \lambda^2} \begin{pmatrix} 1 & -\lambda & 0 \\ -\lambda & 1 & 0 \\ 0 & 0 & 1 + \lambda \end{pmatrix}. \quad (37)$$

The values for λ are obtained by solving (25). The roots of this fourth order polynomial can be determined analytically using Ferrari's method [17, p. 22] and are given in [1, p. B945]. For \mathbf{p} we subsequently find $\mathbf{p} = \mathbf{\Lambda}^{-1}\mathbf{d}$, or more explicitly

$$p_{11} = \frac{\lambda d_{22} - d_{11}}{\lambda^2 - 1}, \quad p_{22} = \frac{\lambda d_{11} - d_{22}}{\lambda^2 - 1}, \quad p_{12} = \frac{d_s}{1 - \lambda}. \quad (38)$$

2.3 J_B -Optimization

In [2, p. 131-133] a *projection method* (PM) has been proposed for the minimization of (9b). As our numerical results will show, this method proves insufficient for some examples. Therefore we developed two improved methods, viz., the *segmented projection method* (SPM) and the *segmented arc length method* (SALM). Before we introduce the boundary methods, we first introduce some notation.

Let $\mathbf{x}_{ij} = ((x_1)_i, (x_2)_j) \in \mathcal{X}$ be the grid points of a Cartesian grid with $i = 1, \dots, N_{x_1}$ and $j = 1, \dots, N_{x_2}$ denoting the first and second coordinate, respectively. Let \mathbf{x}_l be the grid points restricted to $\partial\mathcal{X}$ for $l = 1, \dots, N$. We index $\mathbf{x}_l = 1, \dots, N$ in the clockwise direction such that $\mathbf{x}_1 = \mathbf{x}_{1,1}$, i.e. the first point on $\partial\mathcal{X}$ equals the point \mathbf{x}_{ij} with $i = j = 1$. We approximate $\mathbf{m}_{ij} \approx \mathbf{m}(\mathbf{x}_{ij})$, $\mathbf{m}_l \approx \mathbf{m}(\mathbf{x}_l)$ and similarly for the other variables.

The main idea behind SPM and SALM is to partition the boundaries of the source and target domains in segments. We then uniquely enforce one source segment to be mapped to one target segment. We then distribute \mathbf{b}_l , corresponding to \mathbf{m}_l by either a projection (SPM) or by a ratio of arc lengths (SALM).

Let the boundary segments of \mathcal{X} be the curves $\Gamma_k^{\mathcal{X}} \subset \partial\mathcal{X}$ such that for N_Γ boundary segments we have $\cup_{k=1}^{N_\Gamma} \Gamma_k^{\mathcal{X}} = \partial\mathcal{X}$. We denote $\Gamma_{N_\Gamma+1}^{\mathcal{X}} = \Gamma_1^{\mathcal{X}}$ and assume the intersections $\Gamma_{k_1}^{\mathcal{X}} \cap \Gamma_{k_2}^{\mathcal{X}}$ contain precisely one element if $k_2 = k_1 + 1$ and no elements otherwise. Furthermore, we require each $\Gamma_k^{\mathcal{X}}$ to be parametrizable. We assume similar properties for $\Gamma_k^{\mathcal{Y}}$. We aim to map each boundary segment of $\partial\mathcal{X}$ to a boundary segment of $\partial\mathcal{Y}$, hence we enforce $\mathbf{m}(\Gamma_k^{\mathcal{X}}) = \Gamma_k^{\mathcal{Y}}$ for $k = 1, \dots, N_\Gamma$, from which it follows that

$$\mathbf{m}(\partial\mathcal{X}) = \mathbf{m}(\cup_{k=1}^{N_\Gamma} \Gamma_k^{\mathcal{X}}) = \cup_{k=1}^{N_\Gamma} \mathbf{m}(\Gamma_k^{\mathcal{X}}) = \cup_{k=1}^{N_\Gamma} \Gamma_k^{\mathcal{Y}} = \partial\mathcal{Y}, \quad (39)$$

which is the required transport boundary condition.

Figure 1 shows a part of $\partial\mathcal{Y}$ and (parts of) three boundary segments. In the following we fix k and for brevity drop the subscript in $\Gamma_k^{\mathcal{X}}$ and $\Gamma_k^{\mathcal{Y}}$.

Let \mathbf{y}_i for $i = 1, \dots, N_b$ be a discretization of the boundary segment $\Gamma^{\mathcal{Y}}$ such that for a given counter clockwise parametrization $\mathbf{y}(s) : [0, 1] \rightarrow \Gamma^{\mathcal{Y}}$, we have $\mathbf{y}_1 = \mathbf{y}(0)$ and $\mathbf{y}_{N_b} = \mathbf{y}(1)$. We choose to parametrize $\partial\mathcal{X}$ and $\partial\mathcal{Y}$ in opposite directions because \mathbf{m} reverts the direction if it is a solution to the hyperbolic Monge-Ampère.

Projection method. We briefly explain PM as introduced by [2, p. 131-133]. We perform the following for each approximation \mathbf{m}_l individually. Let $N_\Gamma = 1$, i.e., we consider the whole boundary as one boundary segment. Furthermore, let $\mathbf{y}_{N_b+1} = \mathbf{y}_1$, we connect adjacent points \mathbf{y}_i and \mathbf{y}_{i+1} by straight line segments. The projection of \mathbf{m}_l onto the line connecting \mathbf{y}_i and \mathbf{y}_{i+1} is given by

$$\mathbf{m}_i^P(t_i) = \mathbf{y}_i + t_i(\mathbf{y}_{i+1} - \mathbf{y}_i), \quad (40a)$$

$$t_i = \frac{(\mathbf{m}_l - \mathbf{y}_i) \cdot (\mathbf{y}_{i+1} - \mathbf{y}_i)}{|\mathbf{y}_{i+1} - \mathbf{y}_i|^2}. \quad (40b)$$

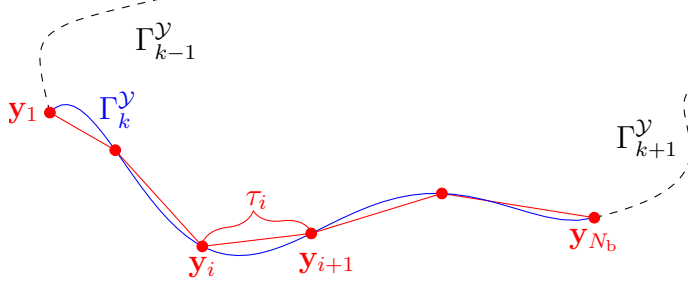


Figure 1: Schematic overview of the discretization of $\partial\mathcal{Y}$.

As only $0 \leq t_i \leq 1$ corresponds to a point on the line segment between \mathbf{y}_i and \mathbf{y}_{i+1} , we limit t_i according to $\hat{t}_i = \min(1, \max(0, t_i))$. Among all possible line segments, we choose \mathbf{b}_l corresponding to \mathbf{m}_l , such that the distance is smallest, i.e.,

$$i_{\min} = \underset{i}{\operatorname{argmin}} \{ |\mathbf{m}_i^{\text{P}}(\hat{t}_i) - \mathbf{m}_l| \}, \quad (41a)$$

$$\mathbf{b}_l = \mathbf{m}_{i_{\min}}^{\text{P}}(\hat{t}_{\min}). \quad (41b)$$

Segmented projection method. Let $\Gamma_k^{\mathcal{X}} \subseteq \partial\mathcal{X}$ and $\Gamma_k^{\mathcal{Y}} \subseteq \partial\mathcal{Y}$ be boundary segments of the source and target, respectively. For this method, we apply PM to the individual boundary segments instead of the whole boundary at once. Furthermore, we set

$$\mathbf{b}(\Gamma_k^{\mathcal{X}} \cap \Gamma_{k+1}^{\mathcal{X}}) = \Gamma_k^{\mathcal{Y}} \cap \Gamma_{k+1}^{\mathcal{Y}}, \quad 1 \leq k \leq N_{\Gamma} \quad (42)$$

meaning, we map the end points of the source segments to the end points of the corresponding target segments. In practice, these end points are the corners of the source and target domains.

Segmented arc length method. The core idea of this method is as follows: if $\mathbf{m}(\Gamma^{\mathcal{X}}) = \Gamma^{\mathcal{Y}}$, then the arc length of the curve $\mathbf{m}(\Gamma^{\mathcal{X}})$ should be equal to the arc length of the curve $\Gamma^{\mathcal{Y}}$. Numerically we approximate this condition by approximating the arc length of both $\Gamma^{\mathcal{Y}}$ and the distance between the points $\{\mathbf{m}(\mathbf{x}_l) \mid \mathbf{x}_l \in \Gamma^{\mathcal{X}}\}$.

We start with the arc length of the curve $\Gamma^{\mathcal{Y}}$. We approximate the arc length between \mathbf{y}_i and \mathbf{y}_{i+1} along $\Gamma^{\mathcal{Y}}$ by the length of the line segment connecting \mathbf{y}_i and \mathbf{y}_{i+1} . We denote the approximation by

$$\tau_i = |\mathbf{y}_{i+1} - \mathbf{y}_i|, \quad i = 1, \dots, N_b - 1. \quad (43)$$

The approximate cumulative arc length between \mathbf{y}_1 and \mathbf{y}_i in the direction of

increasing s is then given by

$$t_i = \sum_{j=1}^{i-1} \tau_j, \quad i = 1, \dots, N_b. \quad (44)$$

The total arc length from \mathbf{y}_1 to \mathbf{y}_{N_b} is then approximated by $L = t_{N_b}$. We use the cumulative arc lengths to introduce a piece-wise linear interpolation \mathbf{b}_{int} approximating $\mathbf{y}(s)$, viz.

$$\mathbf{b}_{\text{int}}(t) = \mathbf{y}_i + \frac{t - t_i}{t_{i+1} - t_i}(\mathbf{y}_{i+1} - \mathbf{y}_i), \quad t_i \leq t \leq t_{i+1}, \quad (45)$$

where the scalar factor is a scaled coordinate between \mathbf{y}_i and \mathbf{y}_{i+1} . Note that by construction \mathbf{b}_{int} satisfies

$$\mathbf{b}_{\text{int}}(t_i) = \mathbf{y}_i, \quad i = 1, \dots, N_b, \quad (46)$$

and is an approximation of $\partial\mathcal{Y}$.

Next we consider the points $\{\mathbf{m}(\mathbf{x}_l) \mid \mathbf{x}_l \in \Gamma^{\mathcal{X}}\}$. Let N_m be the number of grid points on $\Gamma^{\mathcal{X}}$ such that $\mathbf{x}_l \in \Gamma^{\mathcal{X}}$ for $l = 1, \dots, N_m$. Furthermore, let

$$\sigma_l = |\mathbf{m}_{l+1} - \mathbf{m}_l|, \quad l, \dots, N_m - 1, \quad (47)$$

be an approximation of the arc length from $\mathbf{m}(\mathbf{x}_l)$ to $\mathbf{m}(\mathbf{x}_{l+1})$ along $\partial\mathcal{Y}$. This again introduces a cumulative arc length and a total arc length, respectively, given by

$$s_l = \sum_{j=1}^{l-1} \sigma_j, \quad l = 1, \dots, N_m, \quad \tilde{L} = s_{N_m}. \quad (48)$$

Because \mathbf{m}_l is an approximation and $\Gamma^{\mathcal{Y}}$ is approximated by straight line segments, $\tilde{L} \neq L$ in general. Hence, $s_l \neq L$ may occur such that the end points of $\Gamma^{\mathcal{X}}$ may not be mapped to the end points of $\Gamma^{\mathcal{Y}}$. We fix this by letting

$$\tilde{s}_l = \frac{L}{\tilde{L}} s_l. \quad (49)$$

It follows that $\mathbf{b}_{\text{int}}(\tilde{s}_l)$ forms a proper approximation for \mathbf{m}_l restricted to $\Gamma^{\mathcal{Y}}$, viz.

$$\mathbf{b}_l = \mathbf{b}_{\text{int}}(\tilde{s}_l), \quad l = 1, \dots, N_m. \quad (50)$$

2.4 Grid shock correction

Using the methods outlined above, it is possible that the approximation \mathbf{m}^n of \mathbf{m} contains crossing grid lines, also known as grid shocks [18]. This phenomenon is shown in Figure 2 for an example we discuss in Section 3.2, with grid parameters

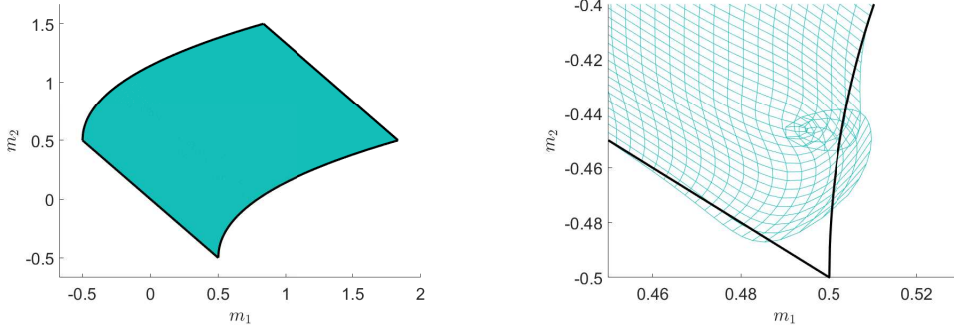


Figure 2: Example of grid shock. The global numerical approximation is shown on the left, and a zoomed-in version on the right.

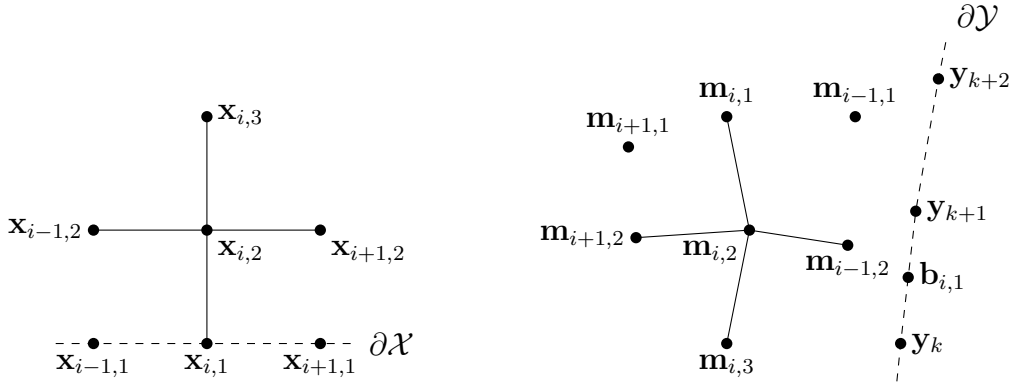


Figure 3: Schematic overview of stencil used for detecting grid shocks. On the right $\mathbf{m}_{i-1,2}$ is closer to $\mathbf{b}_{i,1}$ than $\mathbf{m}_{i,1}$ is, so a grid shock occurs.

$N_{x_1} = N_{x_2} = 321$ after $n = 15,000$ iterations. Though the solution on the left may look visually correct, the grid shock, as seen on the right, prevents proper numerical convergence of our algorithm. To resolve grid shocks, consider a point $\mathbf{x}_{ij} \in \partial\mathcal{X}$ as shown for $j = 1$ in Figure 3 on the left, and the corresponding image \mathbf{m}_{ij} shown on the right. If both \mathbf{m}_{ij} and \mathbf{b}_{ij} are exact, then $|\mathbf{m}_{ij} - \mathbf{b}_{ij}| = 0$ and $|\mathbf{m}_{kl} - \mathbf{b}_{ij}| > 0$ for all $(k, l) \neq (i, j)$. Because both \mathbf{m} and \mathbf{b} are approximated, $|\mathbf{m}_{ij} - \mathbf{b}_{ij}| \neq 0$ in general. To detect grid shocks, we compute the distance $|\mathbf{m}_{ij} - \mathbf{b}_{ij}|$ for all (k, l) such that $|(k, l)^T - (i, j)^T| \leq 2$. If the minimum distance is found for $(k, l) \neq (i, j)$, then we assume a grid shock occurs and we recompute \mathbf{m} . We do so by making α in (9c) dependent on the coordinate, i.e., $\alpha = \alpha(\mathbf{x})$ and $\alpha_{ij} = \alpha(\mathbf{x}_{ij})$ and subsequently reduce α_{ij} on the boundary which puts more emphasis on the minimization of $|\mathbf{m}_{ij} - \mathbf{b}_{ij}|$.

Introducing the \mathbf{x} -dependency, the coefficients α and $1 - \alpha$ in (9c) formally have to be moved inside the integrals of J_I and J_B . After doing so, we compute the first

variation of $J(\mathbf{m}, \mathbf{P}, \mathbf{b}, \alpha) = \frac{1}{2} \iint_{\mathcal{X}} \alpha \|\mathbf{D}\mathbf{m} - \mathbf{P}\|^2 d\mathbf{x} + \frac{1}{2} \oint_{\partial\mathcal{X}} (1 - \alpha) |\mathbf{m} - \mathbf{b}|^2 ds$ w.r.t. \mathbf{m} and apply the fundamental lemma of calculus of variations. Consequently we obtain

$$\nabla\alpha \cdot \nabla m_1 + \alpha \Delta m_1 = \mathbf{p}_1 \cdot \nabla\alpha + \alpha \nabla \cdot \mathbf{p}_1, \quad \mathbf{x} \in \mathcal{X}, \quad (51a)$$

$$(1 - \alpha)m_1 + \alpha \nabla m_1 = (1 - \alpha)\mathbf{b}_1 + \alpha \mathbf{p}_1 \cdot \hat{\mathbf{n}}, \quad \mathbf{x} \in \partial\mathcal{X}, \quad (51b)$$

for the first component of \mathbf{m} . If α is constant in the interior, we have $\nabla\alpha = \mathbf{0}$ in the interior and equations (51) reduce to (12). By analogy, we have (13) for the second component of \mathbf{m} . Let $\alpha_1 \in (0, 1)$. We set $\alpha(\mathbf{x}_{ij}) = \alpha_1$ for \mathbf{x}_{ij} in the interior of \mathcal{X} . For a boundary point $\mathbf{x}_{ij} \in \partial\mathcal{X}$ we instead set

$$\alpha_{ij} = \begin{cases} \alpha_2, & \text{if } \min_{(k,l) \in \mathcal{I}(i,j)} |\mathbf{m}_{kl} - \mathbf{b}_{ij}| < |\mathbf{m}_{ij} - \mathbf{b}_{ij}|, \\ \alpha_1 & \text{otherwise,} \end{cases} \quad (52)$$

where $\mathcal{I}(i, j) = \{(k, l) \mid \mathbf{x}_{kl} \in \text{int}(\mathcal{X}), |(k, l)^T - (i, j)^T| \leq 2\}$ is the space over which we minimize, $\text{int}(\mathcal{X})$ the interior of \mathcal{X} and $\alpha_2 \in (0, \alpha_1)$ a constant. We choose a distance of 2 and the values $\alpha_2 = 0.005$ and $\alpha_1 = 0.2$ since these have proven to work well in practice.

If in the n^{th} iteration we obtain $\alpha(\mathbf{x}) \neq \alpha_1$, we solve (12) and (13) for a second time with the updated α to perform a correction.

Recall, we use a finite difference method for inverting the Poisson equations (12) and (13), yielding a system of equations. This system of equations depends on α . Without grid shock correction, a LU-factorization can be calculated once and used for each subsequent iteration making the inversion of the system efficient. In case $\alpha_{ij} \neq \alpha_1$ for any (i, j) , the same LU-factorization can no longer be used due to the component $\alpha \nabla m_k \cdot \hat{\mathbf{n}}$ in the Robin boundary conditions and a new LU-factorization has to be calculated for the iteration.

3 Numerical results

In this section we present numerical results for five examples. For each example we know the exact solution and compare the numerical methods. We choose $\mathcal{X} = [x_1^m, x_1^M] \times [x_2^m, x_2^M]$, a rectangle which may vary per case. For each example we choose \mathcal{Y} such that it has a unique feature to it. We measure the residual

$$\epsilon_r = \left| D_{x_1}[m_1]_{ij} D_{x_2}[m_2]_{ij} - D_{x_1}[m_2]_{ij} D_{x_2}[m_1]_{ij} + f^2(\mathbf{x}_{ij}, \mathbf{m}_{ij}) \right|_{\infty}, \quad (53)$$

with D_{x_1} and D_{x_2} standard second-order (central in interior and one-sided on boundary) finite difference operators for the first-order derivatives with respect to x_1 and x_2 , respectively. Furthermore, we measure the global discretization errors

ϵ_u , ϵ_{m_1} and ϵ_{m_2} defined by

$$\begin{aligned}\epsilon_u &= |(u_{ij} - u_{11}) - (u(\mathbf{x}_{ij}) - u(\mathbf{x}_{11}))|_\infty, \\ \epsilon_{m_1} &= |(m_1)_{ij} - m_1(\mathbf{x}_{ij})|_\infty, \\ \epsilon_{m_2} &= |(m_2)_{ij} - m_2(\mathbf{x}_{ij})|_\infty,\end{aligned}\tag{54}$$

where the terms u_{11} and $u(\mathbf{x}_{11})$ are introduced due to the nonuniqueness of u given \mathbf{m} ; see the discussion following equations (15). Any fixed grid point could be used, here \mathbf{x}_{11} is chosen. The choice for the ∞ -norm is arbitrary in the sense that any standard norm would give similar results. However, the ∞ -norm is more sensitive to differences in the local errors than, for example, the standard 2-norm. Starting the least-squares algorithm requires an initial guess \mathbf{m}^0 , so we introduce $\tilde{\mathcal{Y}} = [y_1^m, y_1^M] \times [y_2^m, y_2^M]$, the smallest bounding box of \mathcal{Y} . We then choose $\partial\mathbf{m}^0(\mathcal{X}) = \partial\tilde{\mathcal{Y}}$, such that \mathbf{m}_{ij}^0 is equidistantly distributed, i.e., \mathbf{m}_{ij}^0 is the result a bilinear uniform interpolation of the bounding box of \mathcal{Y} with $\det(\mathbf{D}\mathbf{m}^0) < 0$. The initial guess then reads

$$(m_1^0)_{ij} = \frac{(x_1)_{ij} - x_1^m}{x_1^M - x_1^m} y_1^M + \frac{x_1^M - (x_1)_{ij}}{x_1^M - x_1^m} y_1^m,\tag{55a}$$

$$(m_2^0)_{ij} = \frac{x_2^M - (x_2)_{ij}}{x_2^M - x_2^m} y_2^M + \frac{(x_2)_{ij} - x_2^m}{x_2^M - x_2^m} y_2^m.\tag{55b}$$

The initial guess is a (discretized) solution of the hyperbolic Monge-Ampère equation with $f^2 = \text{area}(\mathcal{Y})/\text{area}(\mathcal{X})$, $\mathbf{m} = \nabla u$ and $u = \frac{1}{2}(x^2 - y^2)f$. Three more such initial guesses exist, viz., $u = \frac{1}{2}(y^2 - x^2)f$ and $u = \pm xyf$.

We segmentate the source boundary in segments, clockwise, according to

$$\begin{aligned}\Gamma_1^{\mathcal{X}} &= \{x_1^m\} \times [x_2^m, x_2^M], & \Gamma_2^{\mathcal{X}} &= [x_1^m, x_1^M] \times \{x_2^M\}, \\ \Gamma_3^{\mathcal{X}} &= \{x_1^M\} \times [x_2^m, x_2^M], & \Gamma_4^{\mathcal{X}} &= [x_1^m, x_1^M] \times \{x_2^m\},\end{aligned}\tag{56}$$

and we write

$$\Gamma_k^{\mathcal{Y}} = \left\{ \Gamma_k^{\mathcal{Y}}(s) \mid s \in [0, 1] \right\},\tag{57}$$

for $k = 1, \dots, 4$. Furthermore, we apply grid shock correction only for iteration step $n \geq 100$, as the distance between the boundary of the initial guess and the boundary of the target may be large for small n .

Lastly, we stop the iteration (10) based on the update of \mathbf{m}^n , i.e., based on

$$\Delta m^n = |\mathbf{m}^n - \mathbf{m}^{n-1}|,\tag{58}$$

instead of, the already introduced measures, J_I and J_B . This is because the values for J_I and J_B may stagnate over the iterations while Δm^n is still changing. Conversely, if Δm^n has stagnated, then so have the functionals J_I and J_B . We stop the iterative process when Δm^n reaches floating-point precision.

3.1 Annulus segment

For the first example we consider $\mathcal{X} = [0, 1] \times [-1/2, 1/2]$, $\partial\mathcal{Y} = \cup_{k=1}^4 \Gamma_k^{\mathcal{Y}}$ with

$$\Gamma_1^{\mathcal{Y}}(s) = (\cos(\frac{1}{2} - s), \sin(\frac{1}{2} - s)), \quad (59a)$$

$$\Gamma_2^{\mathcal{Y}}(s) = (e^s \cos(\frac{1}{2}), -e^s \sin(\frac{1}{2})), \quad (59b)$$

$$\Gamma_3^{\mathcal{Y}}(s) = (e \cos(\frac{1}{2} - s), e \sin(s - \frac{1}{2})), \quad (59c)$$

$$\Gamma_4^{\mathcal{Y}}(s) = (e^{1-s} \cos(\frac{1}{2}), e^{1-s} \sin(\frac{1}{2})), \quad (59d)$$

as shown together with the exact mapping on a 21×21 grid in Figure 4 on the left. We choose $\Gamma_k^{\mathcal{Y}} = \nabla u(\Gamma_k^{\mathcal{X}})$ for all examples. Furthermore, this choice of $\Gamma_k^{\mathcal{Y}}$ implies that for SALM and SPM the corners of $\partial\mathcal{X}$ are mapped to the corners of $\partial\mathcal{Y}$. Let $f^2(x_1, x_2) = e^{2x_1}$. The solution is then given by

$$u(x_1, x_2) = e^{x_1} \cos(x_2), \quad (60)$$

which is symmetric in $x_2 = 0$ as can be seen in Figure 4. Unless specified otherwise, we take $N_b = 10^4$ and for each target segment $\Gamma_k^{\mathcal{Y}}$, with $k = 1, \dots, 4$, we construct $\mathbf{y}_i = \Gamma_k^{\mathcal{Y}}(s_i)$ with $s_i = (i-1)/(N_b-1)$ and $i = 1, \dots, N_b$. The results for PM, SPM and SALM are shown in Figure 5 for varying grid configurations with $N_{x_1} = N_{x_2}$. The three figures clearly show second-order convergence of the relevant errors and residual, which is in accordance with the discretization error of the finite difference approximations used. In terms of ϵ_u , PM and SPM ($3 \cdot 10^{-6}$) slightly outperform SALM ($6 \cdot 10^{-6}$) for $N_{x_1} = N_{x_2} = 473$, though the difference is small. Figure 6 shows the J -errors over the iterations on a grid of $N_{x_1} = N_{x_2} = 473$. For PM and SPM we obtained $J_I \approx 2 \cdot 10^{-12}$, $J_B \approx 3 \cdot 10^{-13}$ in approximately 60,000 iterations. SALM gave $J_I \approx 4 \cdot 10^{-12}$, $J_B \approx 7 \cdot 10^{-13}$ in 40,000 iterations. SALM consistently requires less iterations as seen on the left in Figure 7, where the number of required iterations (n_{\max}) for various $N_{x_1} = N_{x_2}$ is shown.

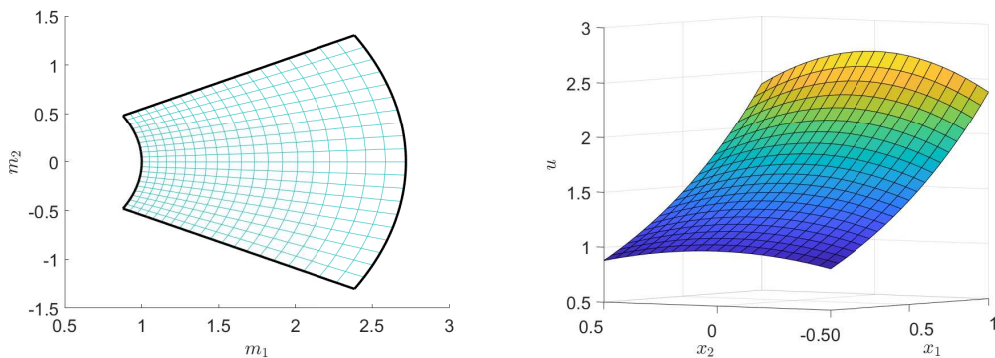


Figure 4: The exact mapping \mathbf{m} (left) and solution u (right) on a 21×21 grid.

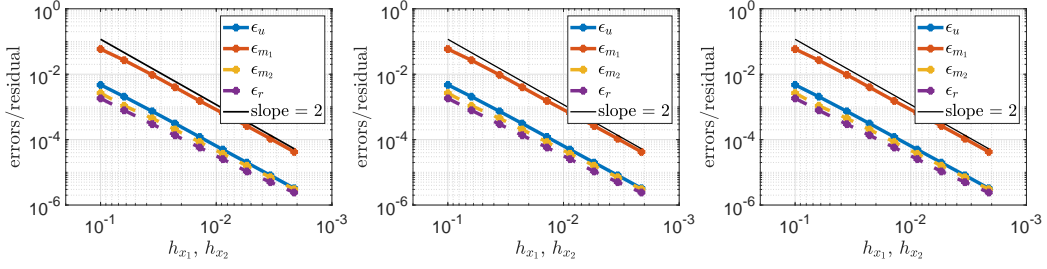


Figure 5: Global error and the residual for PM (left), SPM (middle) and SALM (right).

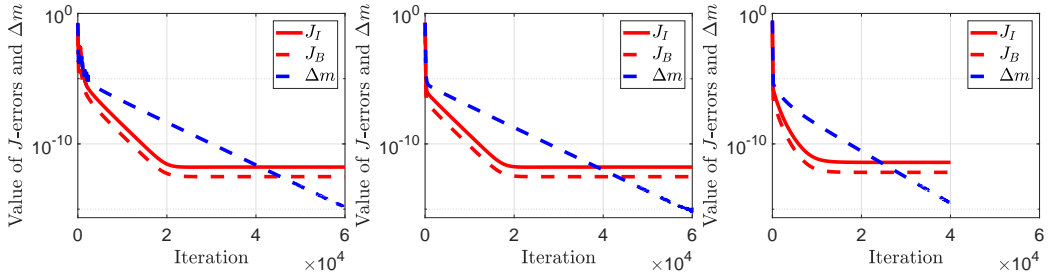


Figure 6: J -errors and Δm over the iterations for PM (left), SPM (middle) and SALM (right).

Convergence of u with respect to N_b is shown on the right of Figure 7 for $N_{x_1} = N_{x_2} = 473$. Two observations are in place. First, for increasing N_b , the error ϵ_u reaches an asymptotic value (dashed black line). This phenomenon is to be expected and occurs when the discretization errors in \mathbf{m}_{ij} , \mathbf{P}_{ij} and u_{ij} , and the finite differences \mathbf{D}_{ij} become dominant, i.e., when the discretization errors due to the choice of N_{x_1} and N_{x_2} dominate the errors due to discretizing the boundary. Secondly, in the regime prior to the asymptote, the discretization error in u due to the boundary discretization is second-order accurate for all three boundary methods.

Finally, the computational cost per iteration for SALM is lowest, second comes SPM and third PM. The projection methods calculate $C \max(N_{x_1}, N_{x_2}) N_b$ projections and performs $C \max(N_{x_1}, N_{x_2})$ searches over N_b points each, with $C \in \mathbb{N}_+$. Similarly, SALM performs a linear interpolation of $C \max(N_{x_1}, N_{x_2})$ points over $N_b - 1$ segments. Therefore, one would expect the average time per iteration to scale linearly in N_x, N_y and N_b for PM and SPM when $N_{x_1} = N_{x_2}$, and N_b is fixed. For SALM, a linear relation is also expected, with a possible asymptote when either the computational load due to $\max(N_{x_1}, N_{x_2})$ or N_b dominates. This is also shown in Figure 8, where, from left to right, $N_{x_1} = N_{x_2} = 501$ is fixed while N_b varies, $N_b = 37$ is fixed and $N_{x_1} = N_{x_2}$ varies, and lastly, $N_b = 10007$ is fixed and $N_{x_1} = N_{x_2}$ varies. Additionally, it is observed that SALM, on average, significantly outperforms the projection methods. Lastly, SPM is approximately

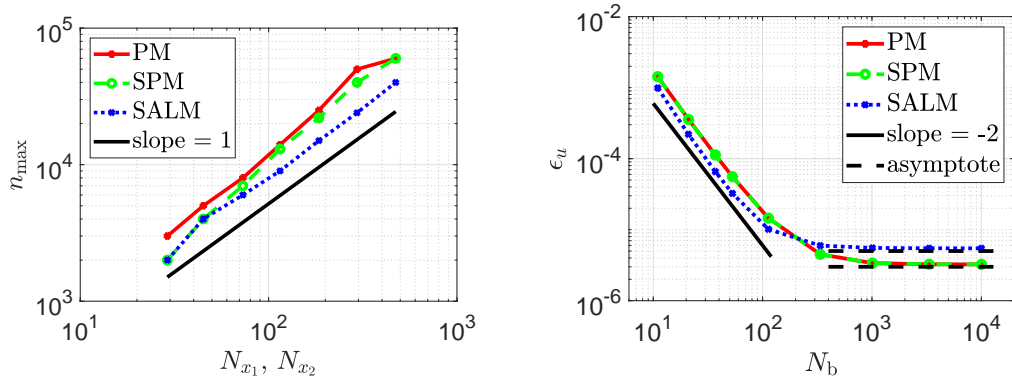


Figure 7: The total number of iterations needed for convergence (left) and the influence of the boundary discretization on ϵ_u (right).

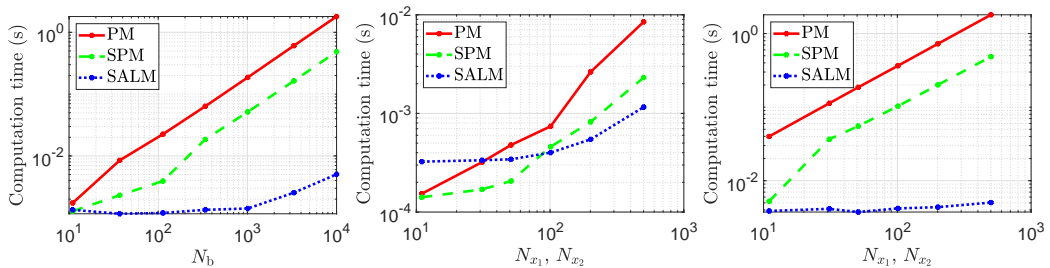


Figure 8: Timing results in seconds for the boundary procedures. On the left, $N_{x_1} = N_{x_2} = 501$ is fixed and in the middle and on the right $N_b = 37$ and $N_b = 10007$, respectively.

four times faster than PM because SPM projects one source segment on a target segment (four times) instead of the whole source boundary on the whole target boundary.

3.2 Deformed square

As a second example we consider a mapping and surface with no symmetries, viz. $\mathcal{X} = [0, 1] \times [-1/2, 1/2]$, $\partial\mathcal{Y} = \cup_{k=1}^4 \Gamma_k^{\mathcal{Y}}$ with

$$\Gamma_1^{\mathcal{Y}}(s) = (s - \frac{1}{2}, -s + \frac{1}{2}), \quad (61a)$$

$$\Gamma_2^{\mathcal{Y}}(s) = (\frac{1}{3}s^3 + s^2 + \frac{1}{2}, s - \frac{1}{2}), \quad (61b)$$

$$\Gamma_3^{\mathcal{Y}}(s) = (-s + \frac{11}{6}, s + \frac{1}{2}), \quad (61c)$$

$$\Gamma_4^{\mathcal{Y}}(s) = (-\frac{1}{3}s^3 + 2s^2 - 3s + \frac{5}{6}, \frac{3}{2} - s), \quad (61d)$$

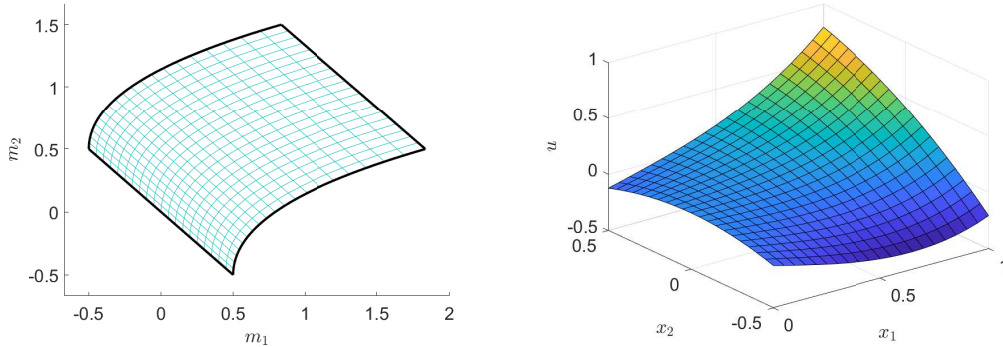


Figure 9: The exact mapping \mathbf{m} (left) and solution u (right) on a 21×21 grid.

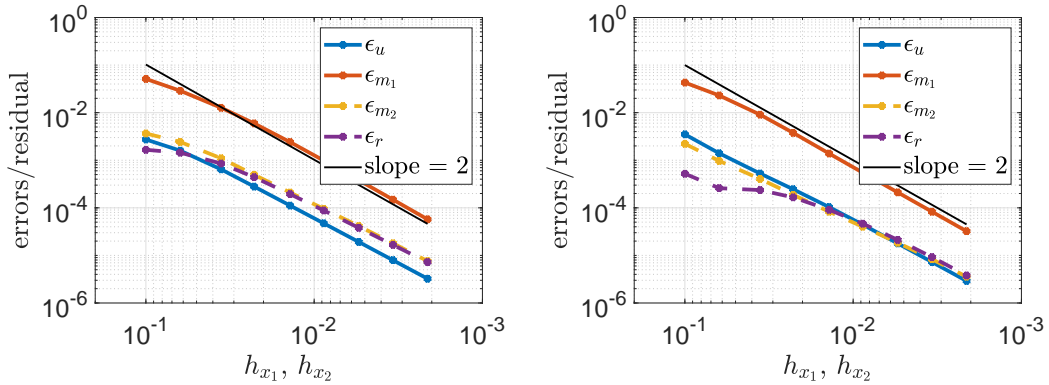


Figure 10: Convergence of the global error and the residual for SPM (left) and SALM (right).

as shown on the left of Figure 9. Let $f^2(x_1, x_2) = (x_1 + 1)^2$, then the exact solution is given by

$$u(x_1, x_2) = \frac{1}{12}x_1^4 + \frac{1}{3}x_1^3 + x_1x_2 - \frac{1}{2}x_2^2, \quad (62)$$

which is shown on the right of Figure 9. In Figure 10 errors and residuals are shown for SPM (left) and SALM (right) for varying grid configurations with $N_{x_1} = N_{x_2}$. Both figures show second-order convergence which is in accordance with the discretization error of the finite difference approximations used. Figure 11 shows the behaviour of J_I , J_B and Δm for SPM and SALM. For SPM, on the left Δm exhibit oscillations starting at 100 iterations. This is due to the grid shock correction, enabled in the 100th iteration. As it turns out, this is one example where grid shocks occur using SPM. Without the grid shock correction, Δm would still go to computer precision but the grid shock (as visualized on the right of Figure 2) would remain and subsequently J_I , J_B and the errors ϵ_u , ϵ_{m_1} and ϵ_{m_2} and the

residual ϵ_r would be three orders of magnitude higher.

Lastly we discuss the results for PM. In Figure 12 the errors J_I and J_B are shown, both with grid shock correction (left) and without (right). Clearly the example with grid shock correction does not converge, the method actually oscillates between intermediate solutions. One may be tempted to think that without grid shock correction the method does work, as Δm goes to machine precision, but this is not the case as shown in Figure 13. The two leftmost figures show the mapping for a 29×29 grid after 50,000 iterations. Clearly, neither of the methods work as intended as there are gaps between the mesh spanned by \mathbf{m}_l and $\partial\mathcal{Y}$, i.e., the transport boundary condition has not been satisfied. The reason why the algorithm with PM does not converge is that the projection of \mathbf{m} onto $\partial\mathcal{Y}$ does not distribute \mathbf{b} well. In particular, no points \mathbf{b}_l near $(0.5, -0.5) \in \partial\mathcal{Y}$ are obtained, as can be seen in Figure 13 on the right, where the blue circles represent \mathbf{m}_l , the red squares \mathbf{b}_l and the thin black lines connect \mathbf{m}_l to \mathbf{b}_l for $l = 1, \dots, N$.

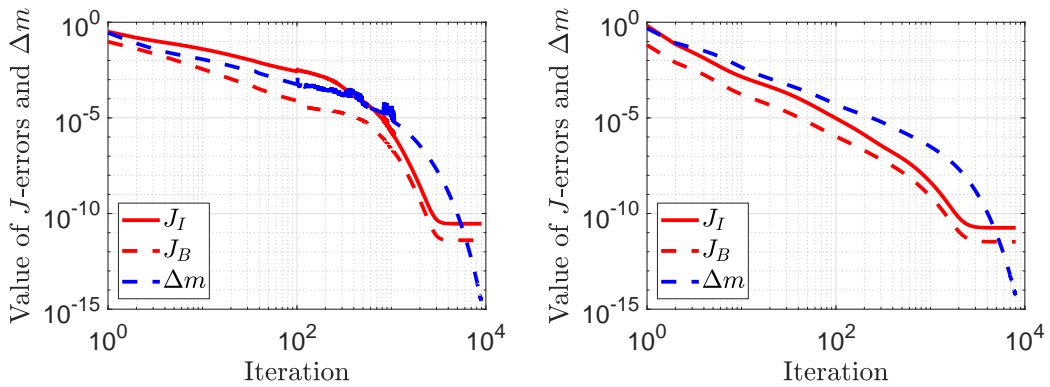


Figure 11: Comparison of J_I , J_B and Δm for SPM (left) and SALM (right) for a grid of 295×295 .

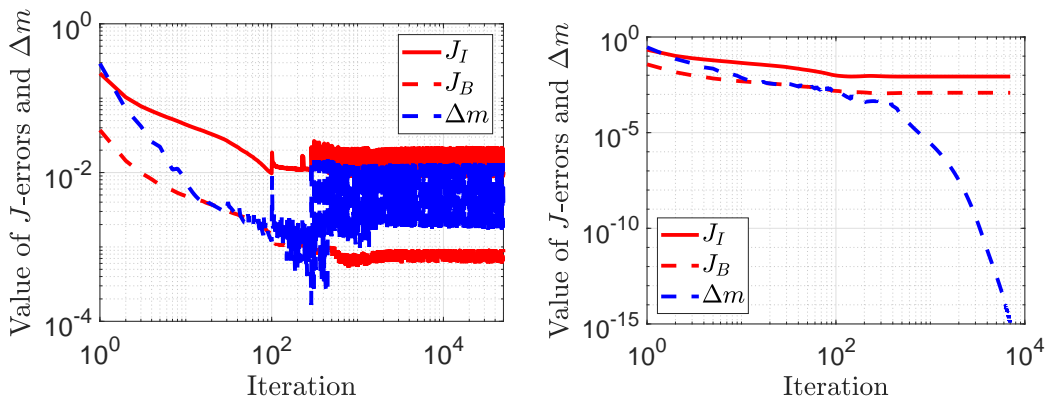


Figure 12: The errors J_I , J_B and the update Δm for PM with shock correction (left) and without (right).

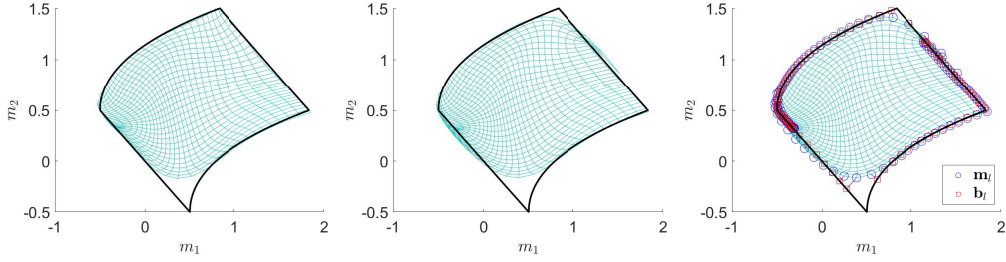


Figure 13: The mapping after 50,000 iterations for PM with shock correction (left) and without (middle) and the accompanying projection of \mathbf{m}_l onto $\partial\mathcal{Y}$ for construction of \mathbf{b}_l without shock correction on the right.

3.3 Inward fold

For this example we consider the target as illustrated in Figure 14, for the exact solution on a 61×61 grid. On the right a zoomed-in version of the target is shown. In the figure we have marked two points, one by a solid circle, and one by an asterisk. The former is a point for which the boundary of the target is not differentiable, while for the latter it is. We will come back to this. The example shown in Figure 14 corresponds to $\mathcal{X} = [0, 1] \times [-1/2, 1/2]$ and $\partial\mathcal{Y} = \cup_{k=1}^4 \Gamma_k^{\mathcal{Y}}$ with

$$\Gamma_1^{\mathcal{Y}}(s) = (0, -\frac{1}{4}s^4 + \frac{1}{2}s^3 - \frac{3}{8}s^2 - \frac{7}{8}s + \frac{31}{64}), \quad (63a)$$

$$\Gamma_2^{\mathcal{Y}}(s) = (\frac{9}{8}s - \frac{1}{2}s^3, -\frac{1}{4}s^4 + \frac{3}{8}s^2 - \frac{33}{64}), \quad (63b)$$

$$\Gamma_3^{\mathcal{Y}}(s) = (-s^3 + \frac{3}{2}s^2 + \frac{1}{4}s + \frac{5}{8}, -\frac{1}{4}s^4 + \frac{1}{2}s^3 + \frac{9}{8}s^2 - \frac{3}{8}s - \frac{25}{64}), \quad (63c)$$

$$\Gamma_4^{\mathcal{Y}}(s) = (-\frac{1}{2}s^3 + \frac{3}{2}s^2 - \frac{19}{8}s + \frac{11}{8}, -\frac{1}{4}s^4 + s^3 - \frac{9}{8}s^2 + \frac{1}{4}s + \frac{39}{64}). \quad (63d)$$

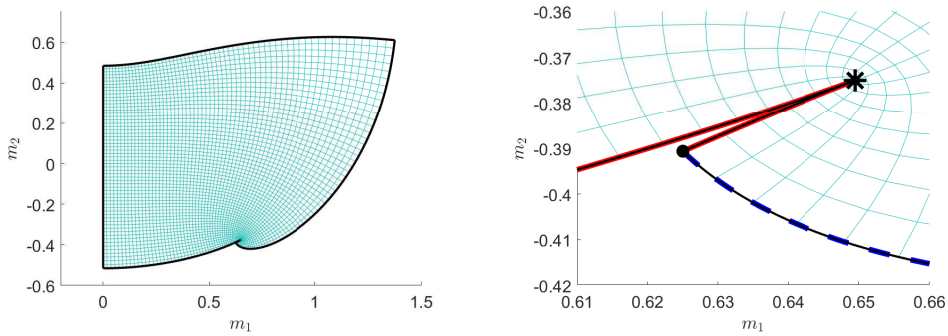


Figure 14: The target domain and mapping, with a zoomed-in version of the Inward fold example.

Furthermore we have

$$f^2(x_1, x_2) = x_1^6 + 3x_1^4x_2^2 + 3x_1^2x_2(x_2^3 - 2) + (1 + x_2^3)^2, \quad (64a)$$

$$u(x_1, x_2) = \frac{x_1^2}{2} - \frac{x_1^4x_2}{4} - \frac{x_2^2}{2} + \frac{x_1^2x_2^3}{2} - \frac{x_2^5}{20}. \quad (64b)$$

Taking derivatives of u yields the mapping, i.e.,

$$m_1(x_1, x_2) = u_{x_1}(x_1, x_2) = x_1 - x_1^3x_2 + x_1x_2^3, \quad (65a)$$

$$m_2(x_1, x_2) = u_{x_2}(x_1, x_2) = -\frac{x_1^4}{4} - x_2 + \frac{3x_1^2x_2^2}{2} - \frac{x_2^4}{4}. \quad (65b)$$

A straightforward calculation shows that $\mathbf{m}(1, 1/2) = (5/8, -25/64)$ which corresponds to the solid circle in Figure 14. Henceforth, \mathbf{m} is not differentiable in the point $(1, 1/2)$ as it is the image of a nondifferentiable (corner) point in \mathcal{X} under a continuously differentiable map. The point depicted by the asterisk originates from the source boundary segment $\Gamma_2^{\mathcal{X}} = [0, 1] \times \{\frac{1}{2}\}$. Let m_1 and m_2 along the boundary be parametrized by s . Then in the point indicated by the asterisk, both $\frac{dm_1(s)}{ds}$ and $\frac{dm_2(s)}{ds}$ change sign. Henceforth, the location of the asterisk can be obtained by solving $\frac{dm_1(s)}{ds} = \frac{dm_2(s)}{ds} = 0$, which is equivalent to

$$\left. \frac{\partial m_1}{\partial x_1} \right|_{x_2=1/2} = 0, \quad \left. \frac{\partial m_2}{\partial x_1} \right|_{x_2=1/2} = 0, \quad 0 \leq x_1 \leq 1. \quad (66)$$

Indeed, doing so one uniquely obtains $x_1 = \sqrt{3}/2$ such that $\mathbf{m}(\sqrt{3}/2, 1/2) = (3\sqrt{3}/8, -3/8)$, which corresponds to the point indicated by an asterisk in Figure 14. Furthermore, smoothness of the boundary in said point is implied.

PM and SPM do not yield converging numerical approximations. Figure 15 shows a zoomed-in version of two numerical solutions for 161×161 grids. The sharp inward fold seems to be the culprit for the boundary method, as is also seen in Figure 16, which shows the projection of \mathbf{m}_l onto $\partial\mathcal{V}$. The figure clearly shows that the method does not pick \mathbf{b}_l deep within the fold and, consequently, the optimization for \mathbf{m} does not produce a mapping with such a sharp fold.

Because SALM does force points \mathbf{b}_l to be located along the whole boundary, naturally points will end up in the fold. This can be seen in Figure 17, where on the left the first iteration of applying SALM to the result of SPM is shown. The 50th iteration of SALM is shown in the middle, showing $\mathbf{m}(\partial\mathcal{X})$ being positioned in the fold. Continuation using SALM yields similar results to using SALM starting from the default initial guess. SALM shows approximately second-order convergence, as graphed on the right of Figure 17, when using (55) as initial guess. SALM does not show any visual distortions, in contrast to PM and SPM.

For the remaining results we will not discuss PM, as it performs, at best, as good as SPM while being more computationally expensive.

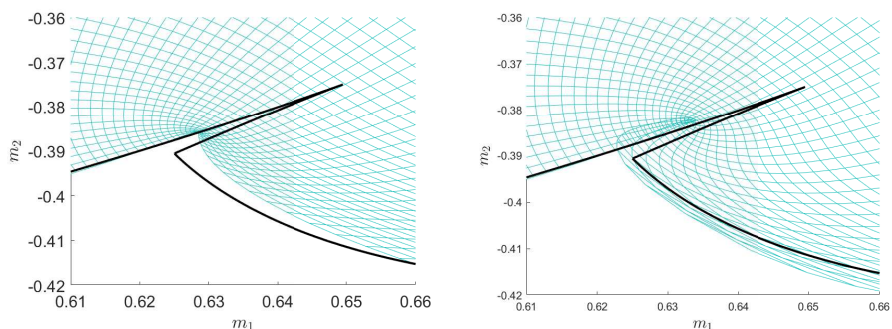


Figure 15: Zoomed-in results for PM (left) and SPM (right) on a 161×161 grid.

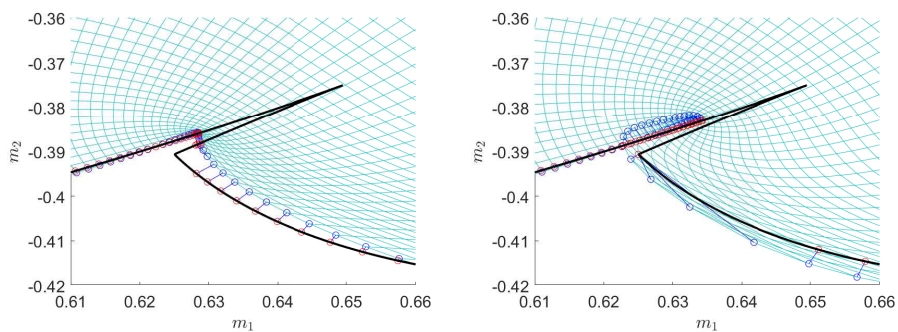


Figure 16: Projection step after convergence for PM (left) and for SPM (right) on a 161×161 grid.

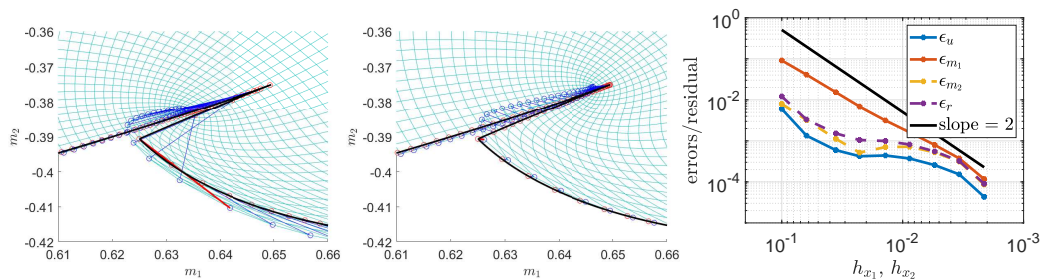


Figure 17: The first (left) and 50^{th} (middle) iteration of continuation by SALM after SPM has converged on a 161×161 grid and the convergence of the errors and residual for SALM starting from a uniform initial guess (right).

3.4 Annulus

For this example we consider the target given in Figure 18, where the central part near $\mathbf{m} = (0, 0)$ is not part of \mathcal{Y} . Let $\mathcal{X} = [0, 2\pi] \times [-1/2, 1/2]$, $\partial\mathcal{Y} = \cup_{k=1}^4 \Gamma_k^{\mathcal{Y}}$ with

$$\Gamma_1^{\mathcal{Y}}(s) = (0, e^{s-\frac{1}{2}}), \quad (67a)$$

$$\Gamma_2^{\mathcal{Y}}(s) = \sqrt{e}(-\sin(2\pi s), \cos(2\pi s)), \quad (67b)$$

$$\Gamma_3^{\mathcal{Y}}(s) = (0, e^{\frac{1}{2}-s}), \quad (67c)$$

$$\Gamma_4^{\mathcal{Y}}(s) = \frac{1}{\sqrt{e}}(\sin(2\pi s), \cos(2\pi s)), \quad (67d)$$

and $f^2(x_1, x_2) = e^{2x_2}$, such that the exact solution is given by

$$u(x_1, x_2) = e^{x_2} \cos(x_1), \quad (68)$$

as shown on the right of Figure 18. Observe that $\mathbf{m}|_{\partial\mathcal{X}}$ is not bijective, as $\Gamma_1^{\mathcal{Y}} = \Gamma_3^{\mathcal{Y}}$. Nevertheless, we introduce both $\Gamma_1^{\mathcal{Y}}$ and $\Gamma_3^{\mathcal{Y}}$ as the orientation, i.e., the parametrization of the segments, matters for SALM.

Figure 19 shows results for SPM. On the left the mapping after the algorithm has converged for a grid with $N_{x_1} = 115$ and $N_{x_2} = 19$. The grid parameters are chosen such that $h_{x_1} \approx h_{x_2}$ as $N_{x_1}/N_{x_2} \approx (x_1^M - x_1^m)/(x_2^M - x_2^m) = 2\pi$. Although the figure on the right clearly shows J_I and J_B have converged, and that Δm reached computer precision, the algorithm does not yield a correct solution, as it does not satisfy the transport boundary condition because there are points \mathbf{m}_{ij} which lie outside \mathcal{Y} , nor does it solve the hyperbolic Monge-Ampère equation as is shown by the residual ϵ_r in Figure 20 on the left.

The reason why SPM does not produce accurate solutions is easiest demonstrated by visualizing a few iterations. To this end, consider the boundary routine for the first, third and tenth iteration as shown in Figure 21. We focus on one segment of the mapping of the boundary, i.e, \mathbf{m}_{ij} with $\mathbf{x}_{ij} \in \Gamma_4^{\mathcal{X}} = [0, 2\pi] \times \{-\frac{1}{2}\}$,

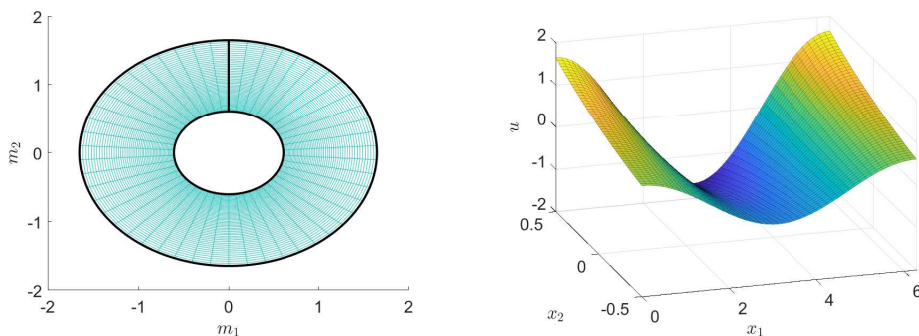


Figure 18: The target and the exact mapping on the left, and the solution surface on the right, both shown on a 51×51 grid.

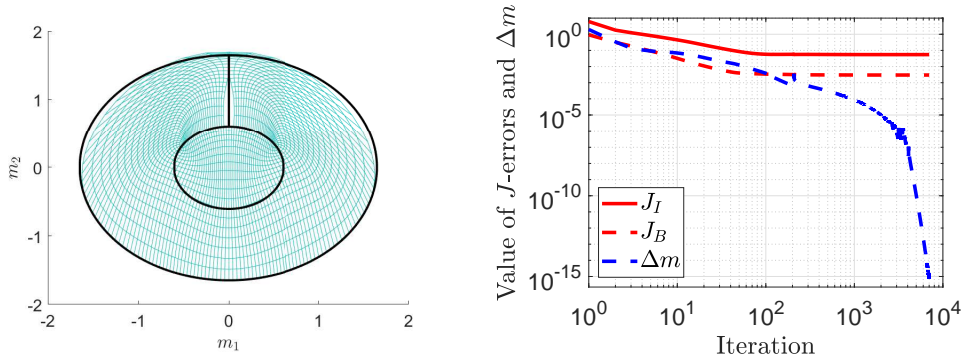


Figure 19: The numerical mapping \mathbf{m} after convergence (left) and the history of J_I , J_B and Δm for SPM.

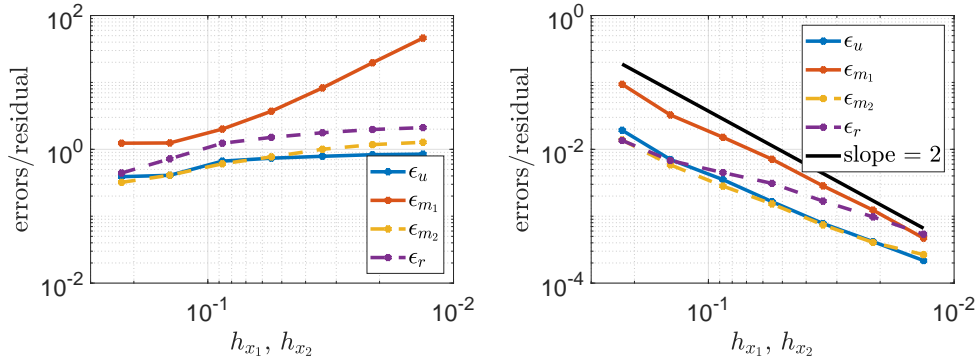


Figure 20: Residual for SPM (left) and SALM (right). No convergence for SPM, and second-order convergence for SALM is observed.

which corresponds to $m_2(0, -\frac{1}{2}) = \exp(-1/2) \approx 0.6$ for the initial guess in Figure 21. For the exact solution, $\Gamma_4^{\mathcal{X}}$ needs to be mapped to the entire inner circle of the target, i.e., $\Gamma_4^{\mathcal{Y}}$. As shown for the first iteration, $\Gamma_4^{\mathcal{X}}$ is mapped to only part of $\Gamma_4^{\mathcal{Y}}$, viz., the accompanying \mathbf{b}_l lies on the northern part of $\Gamma_4^{\mathcal{Y}}$ (the inner circle). In subsequent iterations, shown in the middle and on the right in Figure 21, $\Gamma_4^{\mathcal{X}}$ will again not be mapped to the whole of $\Gamma_4^{\mathcal{Y}}$, as the distance to the northern part of the inner circle remains minimal. This process continues indefinitely.

For SALM such accumulation of \mathbf{b}_l does not occur, as by construction, \mathbf{b}_l is distributed over the boundary segments. The results of the first, second and third iteration of the \mathbf{b} -minimization are shown in Figure 22. Clearly, SALM does not suffer from the same flaws as SPM. As such, the convergence is expected to behave as for the other examples, which is confirmed by the results shown in Figure 20 on the right.

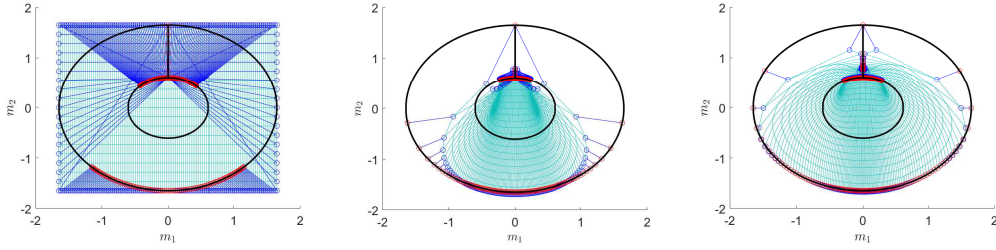


Figure 21: From left to right, the first, third and tenth iteration for SPM.

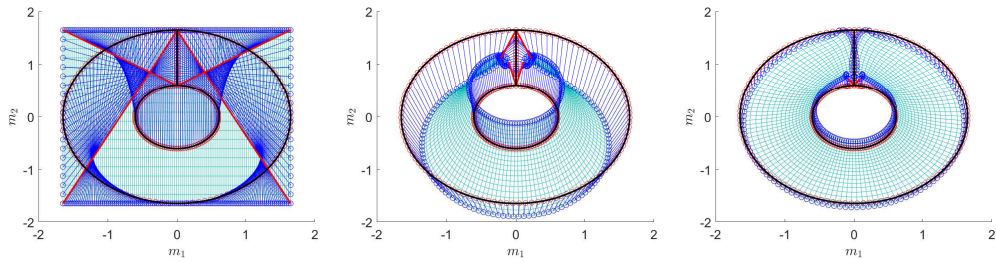


Figure 22: From left to right, the first, second and third iteration for SALM.

3.5 Gradient dependent problem

Lastly we consider an example with f dependent on the gradient of the solution, i.e., $f = f(x_1, x_2, \nabla u)$, viz.

$$f^2(\mathbf{x}, \mathbf{m}) = 3x_2^2 - m_1 \sin(x_1) - \frac{1}{4}m_2^2. \quad (69)$$

We consider the domain $\mathcal{X} = [-1, 1] \times [1, 3/2]$ and $\partial\mathcal{Y} = \cup_{k=1}^4 \Gamma_k^{\mathcal{Y}}$ with

$$\Gamma_1^{\mathcal{Y}}(s) = \left(\frac{\sin(1)}{4}s^2 + \sin(1)s + \sin(1), \cos(1)s + 2\cos(1)\right), \quad (70a)$$

$$\Gamma_2^{\mathcal{Y}}(s) = \left(-\frac{9}{4}\sin(2s-1), 3\cos(2s-1)\right), \quad (70b)$$

$$\Gamma_3^{\mathcal{Y}}(s) = \left(-\frac{\sin(1)}{4}s^2 + \frac{3}{2}s - \frac{9\sin(1)}{4}, -\cos(1)s + 3\cos(1)\right), \quad (70c)$$

$$\Gamma_4^{\mathcal{Y}}(s) = (\sin(2s-1), 2\cos(2s-1)). \quad (70d)$$

The exact solution is given by

$$u(x_1, x_2) = x_2^2 \cos(x_1), \quad (71)$$

and is, together with the mapping and target domain, shown in Figure 23.

By construction of the algorithm, little effort is required for f to be dependent on the mapping \mathbf{m} . The difference being that during the n^{th} iteration, $f^2(\mathbf{x}_{ij}, \mathbf{m}_{ij}^n)$ has to be evaluated instead of $f^2(\mathbf{x}_{ij})$ in the optimization of \mathbf{P} . The results for SPM and SALM with $N_{x_1} = N_{x_2}$ are given in Figure 24, showing second-order convergence for both methods. In this case grid shock correction is needed for SPM to ensure proper convergence.

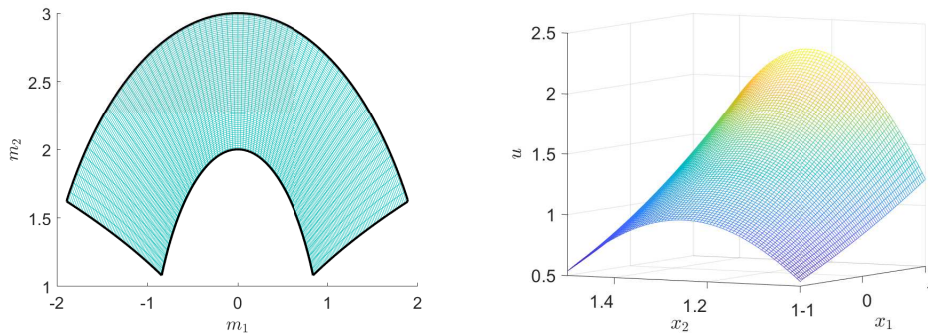


Figure 23: The target and the exact mapping on the left, and the solution surface on the right, both shown on a 51×51 grid.

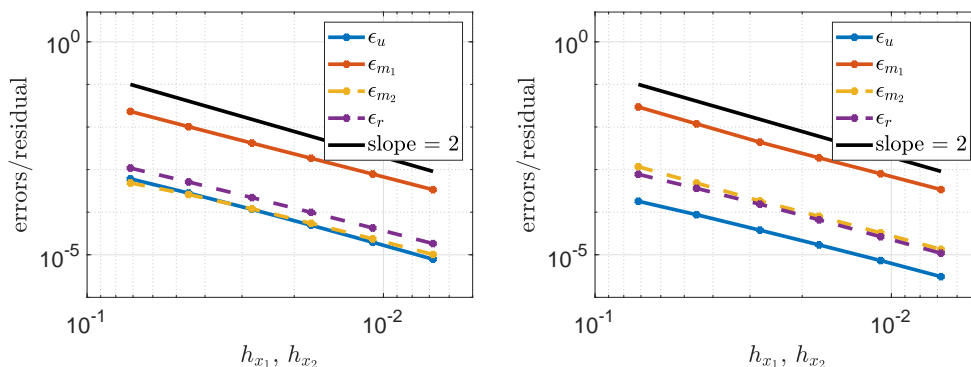


Figure 24: Convergence of SPM (left) and SALM (right).

4 Conclusion

We have introduced a least-squares solver for the hyperbolic Monge-Ampère equation with transport boundary condition. The algorithm, originally introduced by Prins et al. [1] for the elliptic Monge-Ampère equation, has been improved to encompass a more complete description of the roots for the P -optimization. Furthermore, we introduced two new boundary methods. All three boundary methods, if convergent, show second-order convergence of the residual and the global discretization errors as function of the mesh size, and also second-order convergence as function of the number of boundary points. Of the three boundary methods, the *segmented arc length method* is both the only method to converge for all examples and is most computationally efficient, both in terms of computation time per iteration, as in total number of iterations required.

As far as the authors are aware, the least-squares method paired with the *segmented arc length method* for the boundary, is the first method to solve the hyperbolic Monge-Ampère equation with transport boundary conditions.

References

- [1] C. R. Prins, R. Beltman, J. H. M. ten Thije Boonkkamp, W. L. IJzerman, and T. W. Tukker. A least-squares method for Optimal Transport using the Monge–Ampère equation. *SIAM Journal on Scientific Computing*, 37(6):B937–B961, jan 2015.
- [2] C. R. Prins. *Inverse Methods for Illumination Optics*. PhD thesis, Eindhoven University of Technology, 2014.
- [3] H. Ries and A. Rabl. Edge-ray principle of nonimaging optics. *Journal of the Optical Society of America A*, 11(10):2627, October 1994.
- [4] C. Villani. *Optimal Transport: Old and New*. Number 338 in Grundlehren der Mathematischen Wissenschaften. Springer, Berlin, 2009.
- [5] F. Santambrogio. *Optimal Transport for Applied Mathematicians*. Springer International Publishing, 2015.
- [6] Y. Brenier. Décomposition polaire et réarrangement monotone des champs de vecteurs. (French). *R. Acad. Sci. Paris Sér. I Math.*, 305(19):805–808, 1987.
- [7] D. V. Tunitkii. On the global solubility of the Monge–Ampère hyperbolic equations. *Izvestiya: Mathematics*, 61(5):1069–1111, oct 1997.
- [8] J. Hong. The global smooth solutions of Cauchy problems for hyperbolic equation of Monge–Ampère type. *Nonlinear Analysis: Theory, Methods & Applications*, 24(12):1649–1663, June 1995.
- [9] B. S. Westcott and F. Brickell. Computation of reflector surfaces for two-variable beam shaping in the hyperbolic case. *Journal of Physics A: Mathematical and General*, 9(4):611–625, April 1976.
- [10] M. W. M. C. Bertens, E. M. T. Vugts, M. J. H. Anthonissen, J. H. M. ten Thije Boonkkamp, and W. L. IJzerman. Numerical methods for the hyperbolic Monge–Ampère equation based on the method of characteristics. *Partial Differential Equations and Applications*, 3(4):52, Jul 2022.
- [11] L. B. Romijn, J. H. M. ten Thije Boonkkamp, M. J. H. Anthonissen, and W. L. IJzerman. An iterative least-squares method for generated Jacobian equations in freeform optical design. *SIAM Journal on Scientific Computing*, 43(2):B298–B322, January 2021.
- [12] N. K. Yadav, J. H. M. ten Thije Boonkkamp, and W. L. IJzerman. A Monge–Ampère problem with non-quadratic cost function to compute freeform lens surfaces. *Journal of Scientific Computing*, 80(1):475–499, 2019.

- [13] R. Courant and D. Hilbert. *Methods of Mathematical Physics, volume 1*. John Wiley & Sons, Ltd, 1989.
- [14] S Abdallah. Numerical solutions for the pressure Poisson equation with Neumann boundary conditions using a non-staggered grid, I. *J. Comput. Phys.*, 70(1):182–192, May 1987.
- [15] B. D. Froese. A numerical method for the elliptic Monge–Ampère equation with transport boundary conditions. *SIAM Journal on Scientific Computing*, 34(3):A1432–A1459, January 2012.
- [16] L. B. Romijn. *Generated Jacobian Equations in Freeform Optical Design: Mathematical Theory and Numerics*. PhD thesis, Eindhoven University of Technology, 2021.
- [17] Jean-Pierre Tignol. *Galois’ theory of algebraic equations*. World Scientific Publishing, Singapore, Singapore, April 2001.
- [18] J. Cordova and T. Barth. Grid generation for general 2-D regions using hyperbolic equations. In *26th Aerospace Sciences Meeting*. American Institute of Aeronautics and Astronautics, January 1988.